EES Batteries

ROYAL SOCIETY OF CHEMISTRY

PAPER

View Article Online
View Journal

Cite this: DOI: 10.1039/d5eb00127g

Sodium *in situ* modulated phase transition to construct iron/vanadium bimetallic sulfide anodes for "fast-charging" sodium-ion batteries

Tianqi He, Xiaoya Kang, Gaoyang Li, Hao Dang and Fen Ran *

Received 7th July 2025,
Accepted 25th August 2025

DOI: 10.1039/d5eb00127g

rsc.li/EESBatteries

Fast-charging of iron sulfides, as an advanced anode for sodium-ion batteries, is severely restricted by the poor diffusion kinetics of sodium ions and rapid capacity fading. Utilizing the mechanism of *in situ* modulated phase transition of sodium species, herein, iron/vanadium bimetallic sulfides with various phase structures are synthesized to solve this challenge. The presence and content variation of sodium species could effectively adjust the electron density of the Fe atom, thereby implementing the modulation of bimetallic sulfides' phase structure during the sulfidation process. The appropriate phase structure and promising capacitive behavior boost sodium ion transport and reduce capacity attenuation. Consequently, the iron/vanadium bimetallic sulfides exhibit superior sodium storage capacity (424.67 mAh g^{-1} at 0.05 A g^{-1}), a high rate capability of 192.82 mAh g^{-1} at 10 A g^{-1}, and fast sodium ion diffusion kinetics. Furthermore, the assembled full-batteries deliver a remarkable capacity retention of 43.4% after 1200 cycles at 1 A g^{-1}. This work, inspired by the use of sodium as an electron promoter for iron-based catalysts for CO_2 hydrogenation, promises a convergence of catalysis and the synthesis of bimetallic sulfides to achieve fast-charging of sulfides.

Broader context

In recent years, transition metal sulfide anodes have attracted considerable attention, as they are expected to facilitate fast-charging of sodium-ion batteries. Iron sulfides (FeS_2, FeS, $Fe_{1-x}S$, Fe_7S_8, *etc.*) are emerging as a rising star of sodium-ion battery anodes by virtue of abundant resources, plentiful phase structures, electrocatalytic effects of iron elements, and facile synthesis approaches. However, rapid capacity fading, unsatisfactory rate performance, and dissolution of sodium polysulfides hinder their fast-charging. Building bimetallic sulfides is a highly promising strategy to address this challenge. Regrettably, most of the synthetic routes reported for fabricating bimetallic sulfides to advance Na^+ storage are comparatively cumbersome to date. Therefore, it is imperative to exploit facile and scalable methods for synthesizing bimetallic sulfides. Inspired by the use of sodium as an electron promoter to enhance the activity and selectivity of iron-based catalysts for the CO_2 hydrogenation reaction, in this contribution, iron/vanadium bimetallic sulfides with variable phase structures are fabricated *via in situ* modulating phase transformation leveraging the electron-promoting effect of sodium species. As an anode for sodium-ion batteries, the iron/vanadium bimetallic sulfide exhibits promising sodium storage rate behavior (specific capacity is 424.67 mAh g^{-1} at 0.05 A g^{-1} and remains 192.82 mAh g^{-1} at 10 A g^{-1}), desirable capacitive contribution, and rather fast Na^+ diffusion kinetics. Overall, this discovery promises a convergence of catalysis and the synthesis of bimetallic sulfides to achieve fast-charging of sulfides.

1. Introduction

Fast-charging of sodium-ion batteries (SIBs) has attracted considerable attention in recent years, as SIBs are regarded as a potential powertrain for electric vehicles (EVs) and other energy storage systems, echoing societal desire for green economic development.[1,2]The achievement of fast-charging is conducive to developing SIB-based large-scale grid energy storage, and also addressing charging time constraints for EVs when SIBs are employed as power systems.[3,4] Regrettably, fast-charging of SIBs is severely hampered by anode materials.[5,6] Therefore, it is necessary to elaborately design anode materials to boost electrochemical reaction kinetics that could perfectly deliver the virtues of SIBs with fast-charging.[7]

Among numerous anode materials, the restriction factors of fast-charging are varied. Specifically, structural instability and sodium dendrite growth (hard carbon), and narrow interlayer spacing (soft carbon and graphite) are the dominant constraints for carbonaceous materials. The inferior theoretical capacity renders intercalated oxide incapable of achieving high-rate capacity.[5] Severe volume expansion (even higher than

Energy Storage Institute of Lanzhou University of Technology, School of Materials Science and Engineering, State Key Laboratory of Advanced Processing and Recycling of Non-ferrous Metals, Lanzhou University of Technology, Lanzhou 730050, China. E-mail: ranfen@lut.edu.cn, ranfen@163.com

400%) restricts fast-charging of alloy-type materials.[8] In contrast, transition metal chalcogenides, especially transition metal sulfides (TMSs), are expected to realize fast-charging of SIBs given their prominent electrochemical reversibility, attractive theoretical capacity, and relatively smaller volume change.[9,10] Iron sulfides (FeS_2, FeS, $Fe_{1-x}S$, Fe_7S_8, *etc.*) are emerging as a rising star of SIB anodes by virtue of abundant resources, plentiful phase structures, electrocatalytic effects of iron elements, and facile synthesis approaches.[11,12] As with other TMSs, rapid capacity fading, unsatisfactory rate performance, and dissolution of sodium polysulfides hinder fast-charging of iron sulfides.[13,14] To achieve the preeminent fast-charging property, considerable effort has been devoted to modifying iron sulfides, such as carbon encapsulation,[15,16] heteroatom doping,[13] construction of heterojunctions,[11] *etc.*, so as to reduce volume expansion, enhance electrical conductivity, accelerate Na^+ diffusion kinetics, and inhibit the dissolution of sodium polysulfides.[14,15,17,18]

Out of myriad strategies, building bimetallic sulfides is a highly promising approach for enhancing the electrochemical performance of single metal sulfides. It could increase active sites for conversion reactions, provide a narrow band gap and improved electronic conductivity, and achieve satisfactory specific capacity and long cycling lifespan attributed to the buffering effect of isolated nanostructures created during the first charging/discharging cycle.[7,19,20] Combined with these merits, bimetallic sulfides exhibit exceptional electrochemical capability.[21] A representative example is employing $MnCo_2S_4$ as the anode of SIBs. The electrochemistry investigation indicates that $MnCo_2S_4$ possesses superb sodium storage performance, especially surface capacitive behavior (from 73.4% to 94.1%), prolonged cycling lifespan (>800 cycles), and high rate capability (416 mAh g^{-1} at 10 A g^{-1}).[22] Regrettably, most of the synthetic routes reported for fabricating bimetallic sulfides to advance Na^+ storage are comparatively cumbersome to date.[23] Besides, Na^+ storage is also hindered by side reactions arising from the nanostructures of materials.[24] It should be highlighted that the capacitive behavior of anode materials is indispensable to achieving fast-charging.[10,22,25,26] Consequently, it is of considerable significance to develop iron-based bimetallic sulfide anodes using a simple synthetic route along with enriched capacitive behavior, which could rectify the inherent defects of iron sulfides, thereby realizing fast-charging of SIBs.

Herein, iron/vanadium bimetallic sulfides with variable phase structures are fabricated *via in situ* modulating phase transformation leveraging the electron-promoting effect of sodium species, inspired by the use of sodium as an electron promoter enhancing the activity and selectivity of iron-based catalysts for the CO_2 hydrogenation reaction.[27,28] This is successfully accomplished relying on the dual contribution of sodium vanadate ($NaVO_3$). Firstly, $NaVO_3$ contributes a vanadium source for fabricating bimetallic sulfides, which is favorable for introducing surface capacitive behaviors.[29] Then, the sodium in $NaVO_3$ serves as an electron promoter to guarantee the *in situ* modulation of phase structure to synthesize varied sulfides during sulfidation. The *in situ* modulation of phase transition is convincingly testified using thermogravimetry coupled with Fourier transform infrared spectroscopy, *ex situ* X-ray diffraction, and X-ray photoelectron spectroscopy. Simultaneously, electrochemistry exploration verifies that iron/vanadium bimetallic sulfide ($V_{1.87}FeS_4$, the mass ratio of ferric nitrate nonahydrate to $NaVO_3$ is 2 : 1) exhibits promising sodium storage rate behavior (specific capacity is 424.67 mAh g^{-1} at 0.05 A g^{-1} and remains 192.82 mAh g^{-1} at 10 A g^{-1}), desirable capacitive contribution (86.48% at 0.1 mV s^{-1}), and rather fast Na^+ diffusion kinetics. Moreover, the full-batteries assembled with $Na_3V_2(PO_4)_3$/C also exhibit remarkable electrochemical properties (capacity retention is 43.4% at 1 A g^{-1} after 1200 cycles). Inspired by the field of catalysis, this work creates a simple and scalable idea for preparing bimetallic sulfides with fast-charging ability.

2. Experimental section

2.1. Chemicals and materials

Ferric nitrate nonahydrate ($Fe(NO_3)_3{\cdot}9H_2O$) was purchased from Tianjin Kaixin Chemical Industry Co., Ltd. Sodium vanadate ($NaVO_3$), ammonium vanadate (NH_4VO_3), and polyvinylpyrrolidone (PVP, K30) were provided by Aladdin®. Sublimed sulfur was obtained from Guangdong Canrd New Energy Technology Co., Ltd. $Na_3V_2(PO_4)_3$/C was provided by Shenzhen Kejing Star Technology Company. All reagents were used directly without any pre-treatment.

2.2. Preparation of iron/vanadium bimetallic sulfides

Firstly, 2.0 g of PVP, K30 was dissolved in 60 mL of deionized water and stirred to obtain a clear solution. Following this, $Fe(NO_3)_3{\cdot}9H_2O$ and $NaVO_3$ were added to the PVP solution with different mass ratios and stirred continuously for 1 h. Subsequently, the above solution was transferred to a 90 °C oven for 24 h to obtain the powders named Fe : V = 1 : 0, Fe : V = 2 : 1, Fe : V = 1 : 1, and Fe : V = 1 : 2, respectively, according to the feeding ratio (mass) of $Fe(NO_3)_3{\cdot}9H_2O$ and $NaVO_3$. Secondly, Fe : V = 2 : 1, Fe : V = 1 : 1, and Fe : V = 1 : 2 were washed with distilled water four times and dried in an oven at 80 °C. Finally, the above precursor powders and sublimed sulfur were fully ground at a mass ratio of 1 : 3 and placed in a tube furnace with Ar ventilation for 4 h at 155 °C and then heated to 600 °C for 4 h to obtain different sulfides. The sulfurized products of Fe : V = 1 : 0, Fe : V = 2 : 1, Fe : V = 1 : 1, and Fe : V = 1 : 2 corresponded to Fe_7S_8, $V_{1.87}FeS_4$, $V_{2.14}Fe_{0.75}S_4$, and FeS_2/V_2O_3, respectively.

2.3. Materials characterization

The surface functional groups of the samples were tested using the IRTracer-100 instrument (Shimadzu, Japan). The crystal phase structure of the samples was analyzed by high-resolution transmission electron microscopy (HRTEM, JEOL, JEM-F200, Japan) and X-ray diffraction (XRD, DX-2800 diffractometer, China). X-ray photoelectron spectroscopy (XPS, AXIS SUPRA, Shimadzu, Japan) and energy dispersive X-ray spec-

troscopy (EDX) were used to analyze the chemical composition and elemental distribution within the samples. XPS calibration was based on the C 1s components with binding energies of 284.8 or 284.0 eV. The morphology and microstructure of the materials were measured using a field emission scanning electron microscope (FESEM, TESCAN MIRA3, USA) and a transmission electron microscope (TEM, JEOL, JEM-F200, Japan), respectively. Using a specific surface area and aperture analyzer (JW-BK200C, JWGB, Beijing, China), the specific surface area and pore size distributions of the samples were determined. Thermogravimetry coupled with Fourier transform infrared spectroscopy (TG-FTIR) (IRXross + DTG-60, Shimadzu, Japan) and *ex situ* X-ray diffraction (*ex situ* XRD, DX-2800 diffractometer, China) were used to analyze the synthesis mechanism of the materials. The thermal preservation procedure was consistent with the sintering procedure of the tube furnace, and the FTIR data collection began after the 155 °C ramp-up.

2.4. Electrochemical measurements

The electrochemical performances of the as-synthesized materials were tested in half- and full-SIBs (CR2032, assembled in an argon-filled glove box (O_2, H_2O < 0.01 ppm)) by cyclic voltammetry (CV), galvanostatic charging/discharging (GCD), and electrochemical impedance spectroscopy (EIS). For half-batteries, the electrodes were manufactured *via* drying and cutting the current collector coated with slurries into 12 mm discs, and the mass loading of active materials on each electrode was approximately 1.2 mg. The active materials, acetylene black, and polyvinylidene difluoride (PVDF) were dispersed in NMP with a weight ratio of 8 : 1 : 1 and stirred for 12 h to prepare a slurry, which was coated on copper foil as a current collector and dried at 80 °C for 12 h in a vacuum oven. The half-batteries were assembled using the above electrode as a working electrode, sodium metal as a counter electrode, and glass fiber (GF/D 1823, Guangdong Canrd New Energy Technology Co., Ltd) as a separator. The electrolyte used was 1 M $NaPF_6$ in diglyme. The CV tests were conducted on a CHI660E electrochemical workstation (Chenhua, Shanghai, China) at various scan rates with a voltage range of 0.3–3 V. The GCD curves were acquired from a LAND CT2001A battery tester at various current densities in the same voltage range as that of the CV test. The sodium-ion full-batteries were assembled using commercial $Na_3V_2(PO_4)_3$/C as the cathode (aluminum foil as a current collector) and Fe_7S_8 or $V_{1.87}FeS_4$ as the anode. The separator and electrolyte were the same as those of the half-batteries. The GCD measurements were conducted in the voltage range of 1–3.8 V.

3. Results and discussion

Sodium (in the form of Na_2O), as an additive for iron-based catalysts, could suppress the olefin hydrogenation reaction by increasing the electron density of active sites, thereby promoting CO_2 conversion and olefin selectivity.[27,30] Given such utility of sodium species, distinct phase structure iron/vanadium bimetallic sulfides were fabricated using a co-precipitation approach followed by an annealing technique, in which phase transition processes are favored by *in situ* modulation of sodium species (possibly in the form of Na_2S). The sample preparation strategy is graphically shown in Scheme 1. Due to the *in situ* modulation of the sulfidation process by sodium species, diverse iron/vanadium bimetallic sulfides were synthesized as the sodium content was varied. Fe : V = 1 : 0, Fe : V = 2 : 1, Fe : V = 1 : 1, and Fe : V = 1 : 2 were sulfurized as Fe_7S_8 (PDF#29-0723), $V_{1.87}FeS_4$ (PDF#31-0657), $V_{2.14}Fe_{0.75}S_4$ (PDF#31-0656), and FeS_2/V_2O_3 (PDF#42-1340/PDF#34-0187) at 600 °C, respectively. In detail, the precursors contained a series of iron/vanadium compounds, $NaNO_3$ or $NaNO_2$, and $Na_2V_6O_{16}$ (Fig. S1 in the SI) except Fe : V = 1 : 0. This is explained by the fact that a series of reactions may occur when $Fe(NO_3)_3{\cdot}9H_2O$ and $NaVO_3$ are added to deionized water ($Fe(NO_3)_3{\cdot}9H_2O$ is added prior to $NaVO_3$, even though they are added almost simultaneously, Fig. S2 in the SI. After the sulfidation process, sodium species are incorporated into the final materials as a heteroatom after fulfilling the mission of adjusting the phase transition, which is highly preferred for sodium storage (Fig. S3 and Table S1 in the SI).[13] Interestingly, distinct sodium storage behaviors are permitted since sulfides feature differing phase structures and morphologies. $V_{1.87}FeS_4$ offers a high specific capacity, excellent rate performance, and fast-charging capability. Noteworthily, a reasonable crystal structure is very crucial for fast-charging of materials.[31] Therefore, the *in situ* modulation of phase transition employing sodium species is applied with a view to synthesizing iron/vanadium bimetallic sulfide anodes with fast-charging capability for SIBs.

The conjecture that $Fe(NO_3)_3{\cdot}9H_2O$ and $NaVO_3$ react in aqueous solution is validated with the aid of FTIR characteristics (Fig. 1a and b). There are significant alterations of precursor powders' FTIR spectra after the introduction of $NaVO_3$ into the solution, especially in the fingerprint region. The V–O–V (~519 cm^{-1}) and V═O (~1000 cm^{-1}) peaks emerge non-negligibly in the samples of Fe : V = 2 : 1, 1 : 1, and 1 : 2 compared to Fe : V = 1 : 0.[32] In addition, the peak at 577 cm^{-1} observed in Fe : V = 1 : 0 corresponds to the Fe–O band,[33] and the peak at 1419 cm^{-1} in Fe : V = 2 : 1 and 1 : 1 is attributed to $NaNO_3$. These results directly demonstrate the reaction between $Fe(NO_3)_3{\cdot}9H_2O$ and $NaVO_3$. Additionally, the peaks located at 1288 and 1383 cm^{-1} belong to the asymmetrical stretching vibrations of NO_3 and NO_2, respectively. Fig. 1(c) displays the XRD results after sulfidation of different precursors. It was found that the phase structure of the product could be adjusted by altering the mass ratio of Fe and V. Noteworthily, the V_2O_3 phase gradually increased with increasing of $NaVO_3$ in the reaction system. The resultant product after sulfidation was a complex of FeS_2 and V_2O_3 when Fe : V = 1 : 2 as a precursor.

The XPS technique was used to confirm the chemical state of the elements in varied samples. The full spectra indicate that there are obvious peaks of V 2p and Na 1s in $V_{1.87}FeS_4$, $V_{2.14}Fe_{0.75}S_4$, and FeS_2/V_2O_3. Above all, the peak intensities

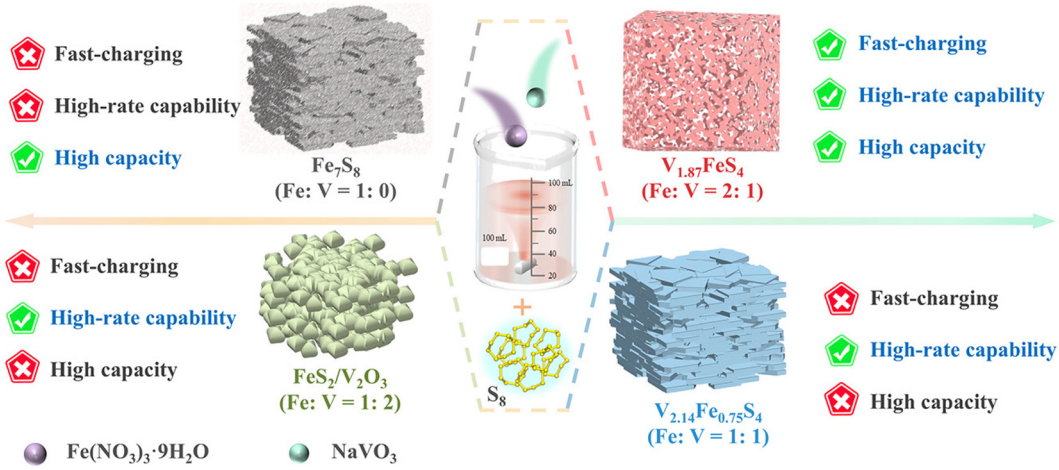

Scheme 1 Schematic illustration of synthesis of different samples with varied sodium storage abilities employing the sodium species *in situ* modulating phase structure.

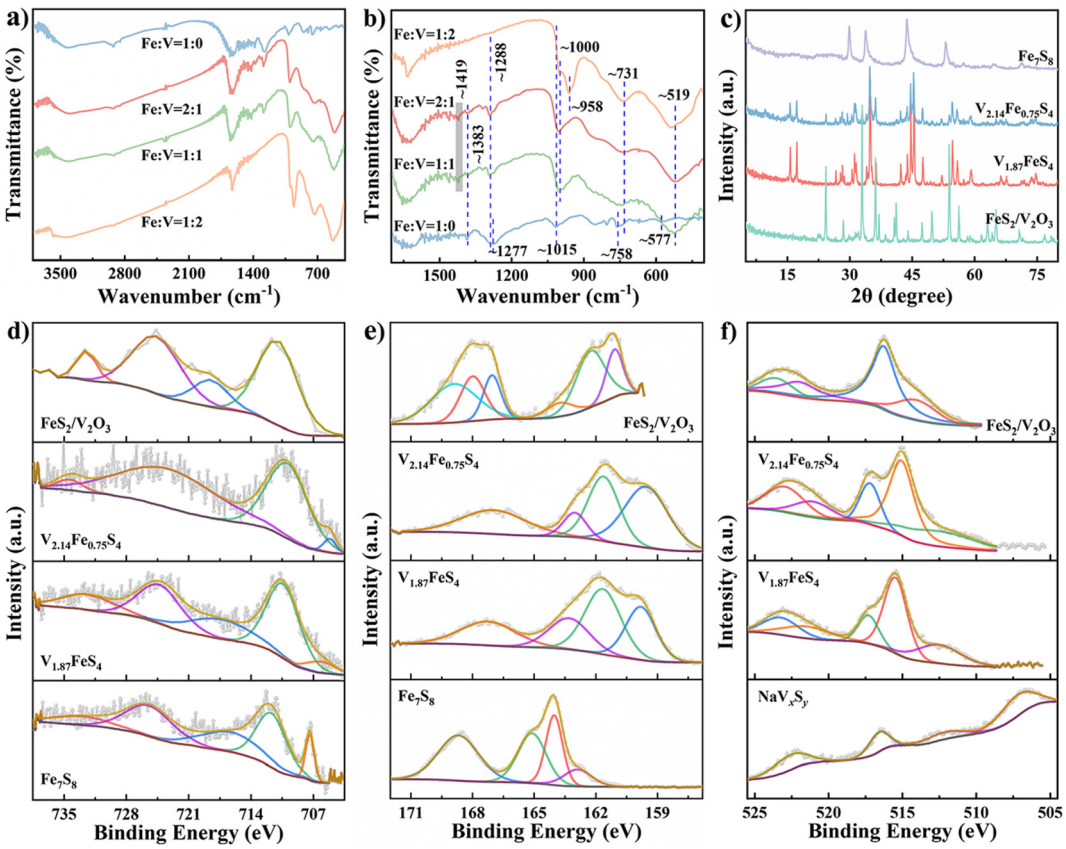

Fig. 1 (a and b) FTIR spectra of different samples before sulfidation, (c) XRD patterns, and (d) Fe 2p, (e) S 2p, and (f) V 2p of Fe_7S_8, $V_{1.87}FeS_4$, $V_{2.14}Fe_{0.75}S_4$, FeS_2/V_2O_3, and NaV_xS_y.

gradually increase with the increasing mass of $NaVO_3$ in the system (Fig. S4 in the SI). The presence of the Na 1s peak supports the hypothesis that sodium is doped as a heteroatom in the samples. Importantly, the high-resolution Fe 2p spectra of varied samples demonstrate marked differences (Fig. 1d). For Fe_7S_8, the high-resolution Fe 2p spectrum primarily features a signal of Fe^{2+} at 707.3 eV (Fe–S bonding) along with a corresponding satellite at 716.2 eV and photoelectron peaks corresponding to Fe^{3+} (711.6 and 725.4 eV).[11–14,17] Obviously, the positions of these fitting peaks in the high-resolution Fe 2p

spectra of $V_{1.87}FeS_4$ and $V_{2.14}Fe_{0.75}S_4$ are apparently shifted toward lower binding energy. This is likely attributed to the effect of sodium species on the electron density of the Fe atom. The fitted peaks for the Fe 2p orbitals of $V_{1.87}FeS_4$ and $V_{2.14}Fe_{0.75}S_4$ appear at 705.1, 709.8, 717.4, 724.2, and 732.3 eV and 706.1, 710.3, 723.2, and 734.3 eV, respectively. The Fe 2p orbital of FeS_2/V_2O_3 is deconvoluted into four peaks, including 710.9, 718.5, 724.6, and 732.5 eV. The Na-doped effect has been reported to weaken the Fe–S bond, as evidenced by the fitting results of S 2P high-resolution XPS spectra of Fe_7S_8 (162.9, 164.0, 165.1, and 168.7 eV), $V_{1.87}FeS_4$ (159.8, 161.7, 163.3, and 167.2 eV), $V_{2.14}Fe_{0.75}S_4$ (159.6, 161.6, 163.0, and 167.0 eV), and FeS_2/V_2O_3 (161.1, 162.3, 163.8, 167.1, 168.0, and 168.9 eV) (Fig. 1e). Significantly, the weakening of the Fe–S bond favors the storage of Na^+ in TMSs.[13] Moreover, $NaVO_3$ is heat-treated with sublimed sulfur at 600 °C (NaV_xS_y), and the V 2p high-resolution XPS spectrum is compared with other samples. It can be observed that the fitted peaks for $V_{1.87}FeS_4$, $V_{2.14}Fe_{0.75}S_4$, and FeS_2/V_2O_3 exhibit a distinct degree of shift toward the higher binding energy, which is probably related to the formation of iron/vanadium bimetallic sulfides or V_2O_3, and some of the sodium species (in $NaVO_3$) are used as promoters to regulate the electron density of the Fe atom.

The crystal structure of the obtained samples could be visualized *via* high-resolution transmission electron microscopy (HRTEM) images. The lattice spacings of 0.241 and 0.319 nm in Fig. 2(a) correspond to the (213) and (−420) crystal planes of Fe_7S_8 from the sulfidation of pure $Fe(NO_3)_3{\cdot}9H_2O$, respectively. The HRTEM images of the as-prepared samples change dramatically after $NaVO_3$ was added to the precursor solution. Specifically, the HRTEM image of $V_{1.87}FeS_4$ indicates a representative lattice spacing of 0.287 nm for the (110) crystal plane; whereas the HRTEM image of $V_{2.14}Fe_{0.75}S_4$ emerges as the (006) crystal plane of V_2O_3, which is ascribed to the existence of a small amount of V_2O_3 in $V_{2.14}Fe_{0.75}S_4$; in addition, the (111) crystal plane of FeS_2 with a lattice spacing of 0.310 nm is present in the HRTEM image of FeS_2/V_2O_3 (Fig. 2b–d). Such results are in accordance with those of XRD, and testify to the effective modulation of the sample crystalline phase during sulfidation. Furthermore, to prove that the sodium species exerts a decisive role in the modulation of the phase structure, $NaVO_3$ was replaced using NH_4VO_3, and the same experiment was carried out with Fe : V = 2 : 1 as a comparison. It was noted that the sulfurized product was in line with that of pure $Fe(NO_3)_3{\cdot}9H_2O$ when NH_4VO_3 was the vanadium source (Fig. S5 in the SI). The result attests that sodium species are not only crucial for modulating phase structures but also a crucial contributor to the formation of iron/vanadium bimetallic sulfides. The high-resolution Fe 2p spectra of Fe : V = 1 : 0 and Fe : V = 2 : 1 further demonstrate that the sodium species modulating the phase structure may be present in the form of Na_2S (Fig. S6 in the SI). This is because the binding energy of all fitted peaks in Fe : V = 2 : 1 is higher than that in Fe : V = 1 : 0 in the high-resolution Fe 2p spectra, whereas it is just the opposite in the corresponding sulfides (Fig. 1d).

In detail, the process of *in situ* modulation of phase structure by virtue of sodium species was investigated using the TG-FTIR technique and *ex situ* XRD. Fig. 2(e–h) show FTIR spectra of Fe_7S_8, $V_{1.87}FeS_4$, $V_{2.14}Fe_{0.75}S_4$, and FeS_2/V_2O_3 during the TGA testing. Similar profiles indicate that the gases volatilized by diverse precursors during the sulfidation under high-temperature are nearly identical. This is also affirmed by the top-view of FTIR spectra during TGA testing (Fig. S7 in the SI). The *ex situ* XRD patterns of each precursor under different sulfidation temperatures reveal their diversity (Fig. 2i–l). The characteristic peaks of sulfur appear in all precursors at 155 °C, with no significant deviation even when held for 4 h, signifying that the formation of sulfides exceeds 155 °C. Continuing to increase the temperature, a pronounced disparity is detectable at 300 °C. The *ex situ* XRD pattern of Fe : V = 1 : 0 at 300 °C is consistent with features at 155 °C (Fig. 2i), while no characteristic sulfur peaks are observed in Fe : V = 2 : 1 and Fe : V = 1 : 1, and even the peaks of $V_{1.87}FeS_4$ and $V_{2.14}Fe_{0.75}S_4$ appear at about 16°, respectively (Fig. 2j and k). In contrast, the characteristic peaks of sulfur in the *ex situ* XRD pattern of Fe : V = 1 : 2 are merely weakened as the temperature rises to 300 °C, probably as a result of fewer substances reacting with sulfur in the system (Fig. 2l). What is more, the compounds in the Fe : V = 1 : 2 system are not fully converted into FeS_2/V_2O_3 even when the temperature rises up to 600 °C, whereas Fe : V = 1 : 0, Fe : V = 2 : 1, and Fe : V = 1 : 1 already possess an identical crystalline structure as the final product at the same temperature. This observation could be interpreted by TGA characterization results. After sulfur diffusion into the interior, Fe : V = 1 : 0 exhibits only a slight mass change at 241 °C, and a greater decline in mass would require an increase in the annealing temperature to about 360 °C, unlike Fe : V = 2 : 1 and Fe : V = 1 : 1, which exhibit a sustained mass decrease after 284 °C and 275 °C, respectively, which is consistent with the considerable change at 300 °C in the *ex situ* XRD patterns. However, Fe : V = 1 : 2 consistently exhibits an inconspicuous mass decline beginning at 275 °C (Fig. 2m). The sulfidation temperature is visibly lower for Fe : V = 2 : 1 and Fe : V = 1 : 1, signifying that the effect of sodium species on the electron density of the Fe atom, in turn, reduces the activation energy of the reaction to generate sulfides. In contrast, the sulfidation of pure $Fe(NO_3)_3{\cdot}9H_2O$ requires relatively high temperatures. Incidentally, it can be found that $NaVO_3$ in Fe : V = 1 : 2 is far in excess based on the reaction conditions, resulting in relatively few substances (same as in Fe : V = 2 : 1 and Fe : V = 1 : 1), which could react with sublimated sulfur at 300 °C. This also accounts for the lack of no apparent variation in *ex situ* XRD and TGA curves of Fe : V = 1 : 2 at 300 °C.

The micro-morphologies of four samples were observed by SEM and TEM, as illustrated in Fig. 3. All samples are micron-sized, and in addition, Fe_7S_8 consists mainly of relatively small particles attached to larger particles. With the gradual introduction of $NaVO_3$ and the modulation of crystalline phase structure with sodium species, the sizes of $V_{1.87}FeS_4$, $V_{2.14}Fe_{0.75}S_4$, and FeS_2/V_2O_3 gradually became smaller, and the structure went from fluffy to smooth. In comparison, $V_{1.87}FeS_4$

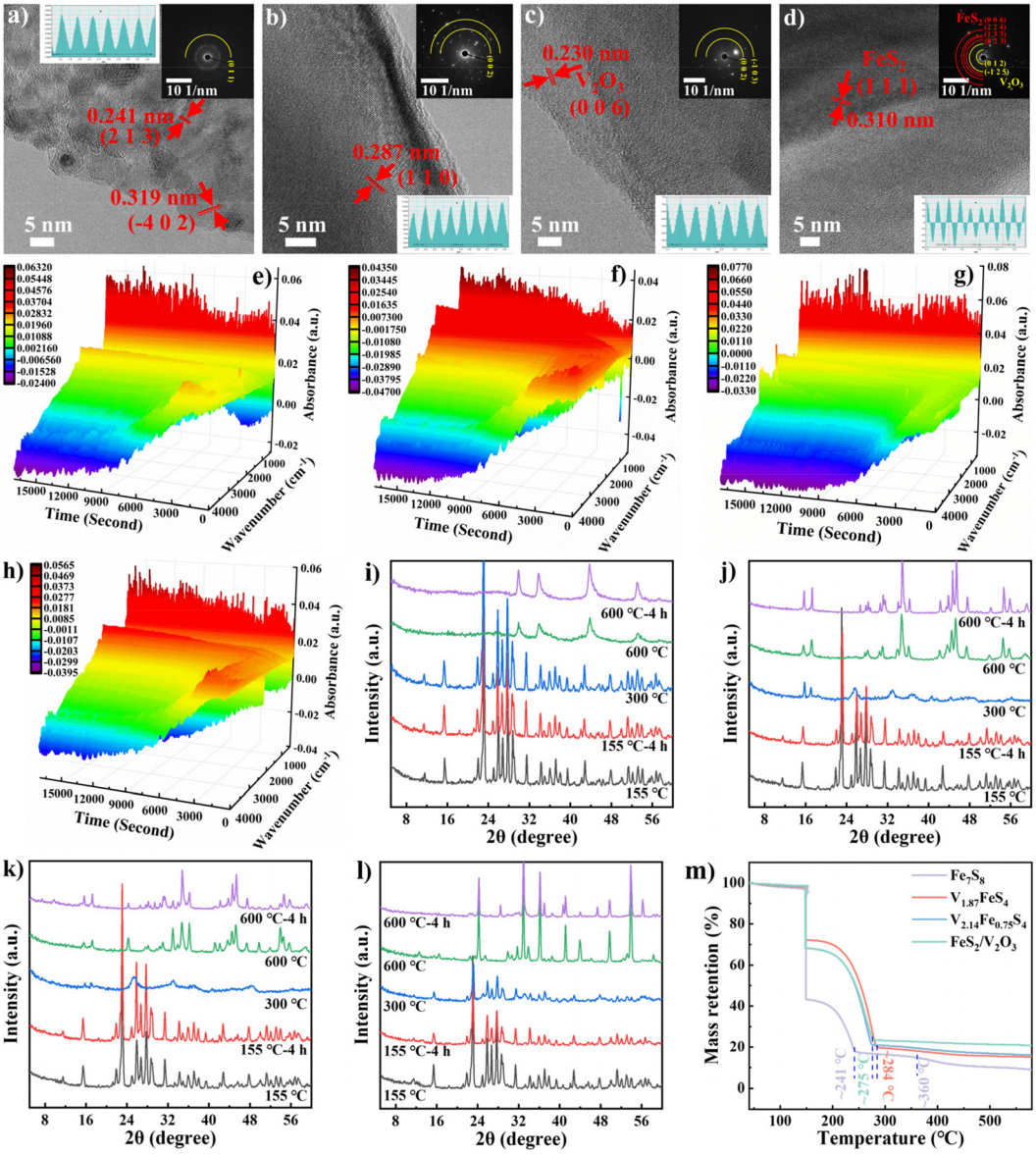

Fig. 2 (a–d) HRTEM and SAED patterns (insets), (e–h) FTIR spectra during the TGA test, (i–l) *ex situ* XRD patterns of different precursors at different sulfidation temperatures, and (m) TGA curves of Fe_7S_8, $V_{1.87}FeS_4$, $V_{2.14}Fe_{0.75}S_4$, and FeS_2/V_2O_3.

possesses a relatively fluffier structure, which is favorable for Na^+ transport (Fig. 3a–d). The regularity of TEM images is similar to that of SEM, that is, FeS_2/V_2O_3 is composed of relatively smaller particles, while the other three samples are composed of a larger bulk (Fig. 3e–h). Meanwhile, EDX mapping results show that Fe and S elements are uniformly distributed in Fe_7S_8, while $V_{1.87}FeS_4$, $V_{2.14}Fe_{0.75}S_4$, and FeS_2/V_2O_3 are mainly composed of uniformly distributed Fe, V, and S elements (Fig. 3i–l). Furthermore, EDX spectroscopy tests revealed the types of elements present in different samples and the percentage of each element's content (Fig. S8 and Table S2 in SI). The analysis of the specific surface area and pore size of different samples further verified the effect of the pore structure and microscopic morphology on the electrochemical performance of the materials (Fig. S9–S10 and Table S3 in the SI). The specific surface area and pore size analyses revealed that the specific surface areas of Fe_7S_8, $V_{1.87}FeS_4$, $V_{2.14}Fe_{0.75}S_4$, and FeS_2/V_2O_3 are 4.444, 9.448, 5.017, and 7.329 $m^2\ g^{-1}$, respectively (Fig. S9 in the SI). Comparatively, $V_{1.87}FeS_4$ owns a higher specific surface area, allowing for the presence of a greater number of Na^+ storage sites, improving the specific capacity of the electrode.[34,35] The pore size distribution of all samples was evaluated by the Barrett–Joyner–Halenda (BJH) method (Fig. S10 in the SI). The mesoporous structure could extend the contact area between the electrolyte and the electrode materials, and mitigate the volume change during charging/discharging, which is conducive to the storage of Na^+.[10]

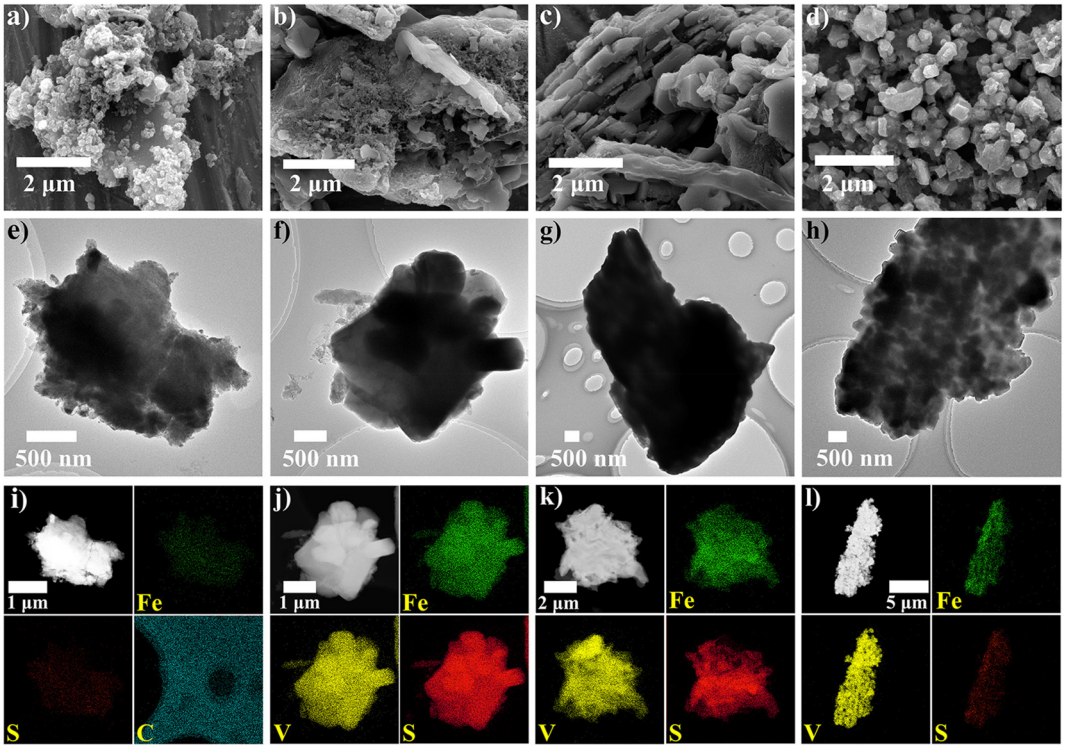

Fig. 3 SEM, TEM, and EDX mapping of (a, e, and i) Fe_7S_8, (b, f, and j) $V_{1.87}FeS_4$, (c, g, and k) $V_{2.14}Fe_{0.75}S_4$, and (d, h, and l) FeS_2/V_2O_3.

The half-batteries were assembled to evaluate the sodium storage behavior of the synthesized samples as SIB anodes in a voltage range of 0.3–3.0 V. The redox peaks in the CV curves of the different samples appear as visible voltage deviations, which arise perhaps from inconsistencies in the crystalline phase structure of samples (Fig. 4a).[36] In the CV curves, it can be observed that after the introduction of vanadium, significant changes occurred in the CV curves of the materials. $V_{1.87}FeS_4$ exhibits weak oxidation peaks at 2.09, 1.51, and 1.26 V and reduction peaks at 0.87 and 1.52 V compared to that of Fe_7S_8. A series of oxidation–reduction peaks mentioned above corresponds to the reactions that occur when the V element stores sodium ions.[37] Furthermore, as the amount of vanadium in the system increases ($V_{2.14}Fe_{0.75}S_4$ and FeS_2/V_2O_3), the intensity of the redox peaks gradually increases. This clearly indicates that vanadium actively participates in the redox process during the electrochemical process and realizes the storage of sodium ions. Meanwhile, GCD curves also show major differences; compared to the other samples, $V_{1.87}FeS_4$ demonstrates the highest stabilized specific capacity at 0.05 A g^{-1} and maintains this superiority until the current density is increased 200-fold (Fig. 4b and c). This preeminent performance may be attributed to the crystal structure of $V_{1.87}FeS_4$, which is far more favorable for Na^+ diffusion and storage. Although the specific capacities of $V_{2.14}Fe_{0.75}S_4$ and FeS_2/V_2O_3 are lower than that of Fe_7S_8 at low current densities, a reversal will occur when the current density is increased to 2 A g^{-1} or even 10 A g^{-1} (Fig. 4c and d). This phenomenon, together with the fact that $V_{1.87}FeS_4$ exhibits admirable sodium storage performance at any current density, firmly certifies that synthesis of bimetallic sulfides or composites could actualize high-rate ability of TMSs.[7,19,38]

Fig. 4(e) reveals the superior rate performance of $V_{1.87}FeS_4$ (45.4%) than Fe_7S_8 (13.4%) when the current density is increased from 0.05 to 10 A g^{-1}, confirming that the creation of iron/vanadium bimetallic sulfides is in favor of addressing the inability to perform fast-charging of iron sulfides. Furthermore, comparison with previously reported bimetallic sulfides reveals that $V_{1.87}FeS_4$ offers exciting Na^+ storage capacity and rate performance (Fig. 4f).[39–42] Fig. 4(g) presents the cycling performances of Fe_7S_8 and $V_{1.87}FeS_4$ at 0.2 A g^{-1}. The batteries were first activated for 5 cycles at a low current density of 0.05 A g^{-1}, and then continuously tested for 100 cycles at 0.2 A g^{-1}. Finally, $V_{1.87}FeS_4$ delivers a specific capacity of 486.62 mAh g^{-1}, while Fe_7S_8 merely achieves a specific capacity of 215.50 mAh g^{-1}. The specific capacities and discharging time of the different samples at varying current densities are listed in Table S4 in the SI. Comparatively, $V_{1.87}FeS_4$ exhibits a much higher specific capacity at the same discharging duration, or a considerably shorter duration for attaining the equivalent specific capacity, justifying a remarkably fast sodium storage trait. The brilliant performance of $V_{1.87}FeS_4$ indicates that fabricating bimetallic sulfides by *in situ* modulation of phase transition of sodium species could effectively overcome the intrinsic defects of Fe_7S_8, thereby realizing the ultrafast Na^+ storage. In order to investigate the stability of the

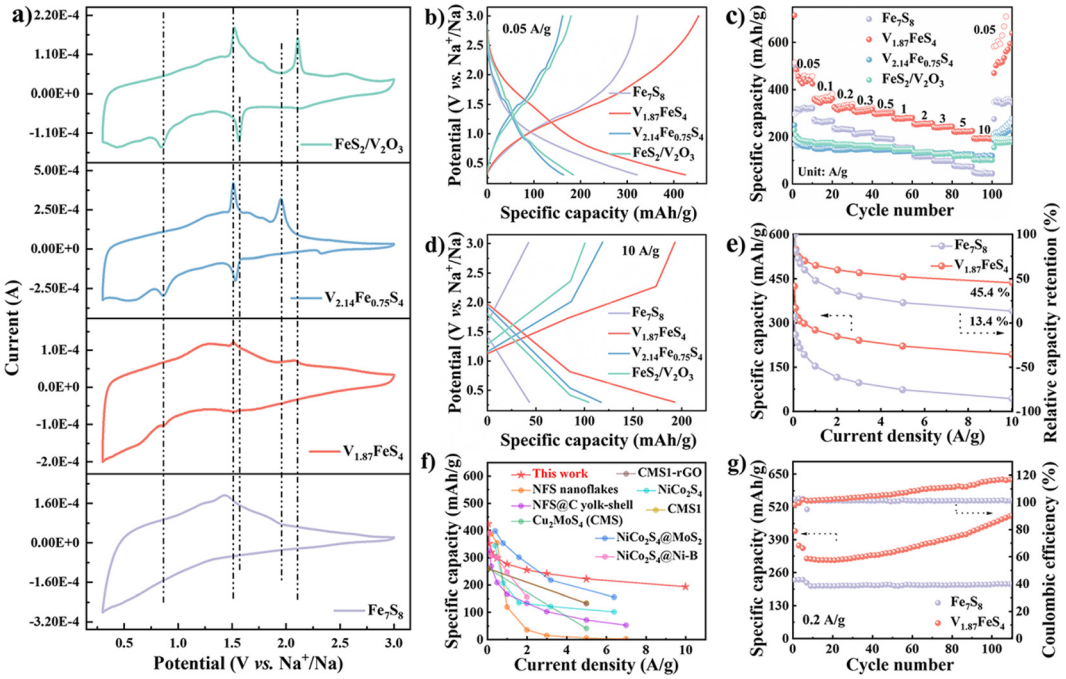

Fig. 4 Comparison of electrochemical performance: (a) CV curves at 0.2 mV s^{-1}, (b) GCD profiles at 0.05 A g^{-1}, (c) rate performance, (d) GCD profiles at 10 A g^{-1} of Fe_7S_8, $V_{1.87}FeS_4$, $V_{2.14}Fe_{0.75}S_4$, and FeS_2/V_2O_3, (e) relative capacity retention at various current densities from 0.05 to 10 A g^{-1} of Fe_7S_8 and $V_{1.87}FeS_4$, (f) comparison with other bimetallic sulfide anode materials for SIBs, and (g) cycling performance of Fe_7S_8 and $V_{1.87}FeS_4$ at 0.2 A g^{-1}.

material during the electrochemical process, scanning electron microscopy characterization is conducted on $V_{1.87}FeS_4$ after a long-term cycling (Fig. S11 in the SI). It can be seen that the microstructure of the material is still maintained during the cycling process, except for forming a dense solid electrolyte layer on the material surface.

The electrochemical performance of $V_{1.87}FeS_4$ is comprehensively analyzed after identifying that it exhibits optimal sodium storage properties. The GCD profile indicates that $V_{1.87}FeS_4$ exhibits a high and stable specific capacity of 424.67 mAh g^{-1} at 0.05 A g^{-1} for the fifth discharging (Fig. 5a). In comparison, the specific capacities of Fe_7S_8, $V_{2.14}Fe_{0.75}S_4$, and FeS_2/V_2O_3 are only 320.95, 163.35, and 183.98 mAh g^{-1}, respectively (Fig. S12 in the SI). The CV profiles of the first three cycles demonstrate excellent electrochemical reversibility of $V_{1.87}FeS_4$ (Fig. 5b), and a broad oxidation peak of around 1.5 V associated with electrochemical reactions occurring in the iron compound, which also appears in the CV curve of Fe_7S_8 (Fig. S13 in the SI).[13,36,43] Also, multiple pairs of redox peaks are evident in CV curves of $V_{2.14}Fe_{0.75}S_4$ and FeS_2/V_2O_3 with increasing V element content (Fig. S13 in the SI), which corresponds to a series of reactions occurring with Fe and V species during sodium storage, respectively.[12,37,44,45] The GCD profiles at varied current densities suggest that $V_{1.87}FeS_4$ possesses splendid sodium storage capacity as well as favorable reversibility compared to the other three samples (Fig. 5c and S14 in the SI). Strikingly, the highly superior specific capacity at 10 A g^{-1} proves the fast-charging nature of $V_{1.87}FeS_4$, thus stimulating an exhaustive investigation of the electrochemical reaction kinetics of samples.

$$i = a \times v^b \quad (1)$$

$$i\,(\mathrm{V})/v^{1/2} = k_1 v^{1/2} + k_2 \quad (2)$$

The capacitive-controlled electrochemical reaction process exhibits faster reaction kinetics compared to that of the diffusive-controlled reaction, favoring Na^+ diffusion. Therefore, the capacitive- and diffusive-controlled contributions of different samples were quantified with the help of CV curves at different scanning rates (Fig. 5d and S15 in the SI) according to eqn (1) and (2), where i (V) represents the peak current, v represents the scanning rate, and a and b denote constants. The capacitive contribution of $V_{1.87}FeS_4$ is 86.48% at 0.1 mV s^{-1} (Fig. 5e), whereas Fe_7S_8, $V_{2.14}Fe_{0.75}S_4$, and FeS_2/V_2O_3 only contribute 23.49%, 72.97%, and 57.12%, respectively, at the identical scanning rate (Fig. S16–18 in the SI). Meanwhile, the capacitive contributions gradually increase with the increasing scanning rate and increase to 96.84%, 63.54%, 93.67%, and 88.49%, respectively, for $V_{1.87}FeS_4$, Fe_7S_8, $V_{2.14}Fe_{0.75}S_4$, and FeS_2/V_2O_3 when the scanning rate is up to 3.0 mV s^{-1} (Fig. 5f and S16–18 in the SI). The higher capacitive contributions denote fast diffusion kinetics of Na^+ and excellent reversible sodium storage qualities when $V_{1.87}FeS_4$ is employed as the SIB anode.

Furthermore, the diffusion characteristics of Na^+ in varied samples were examined employing the galvanostatic intermit-

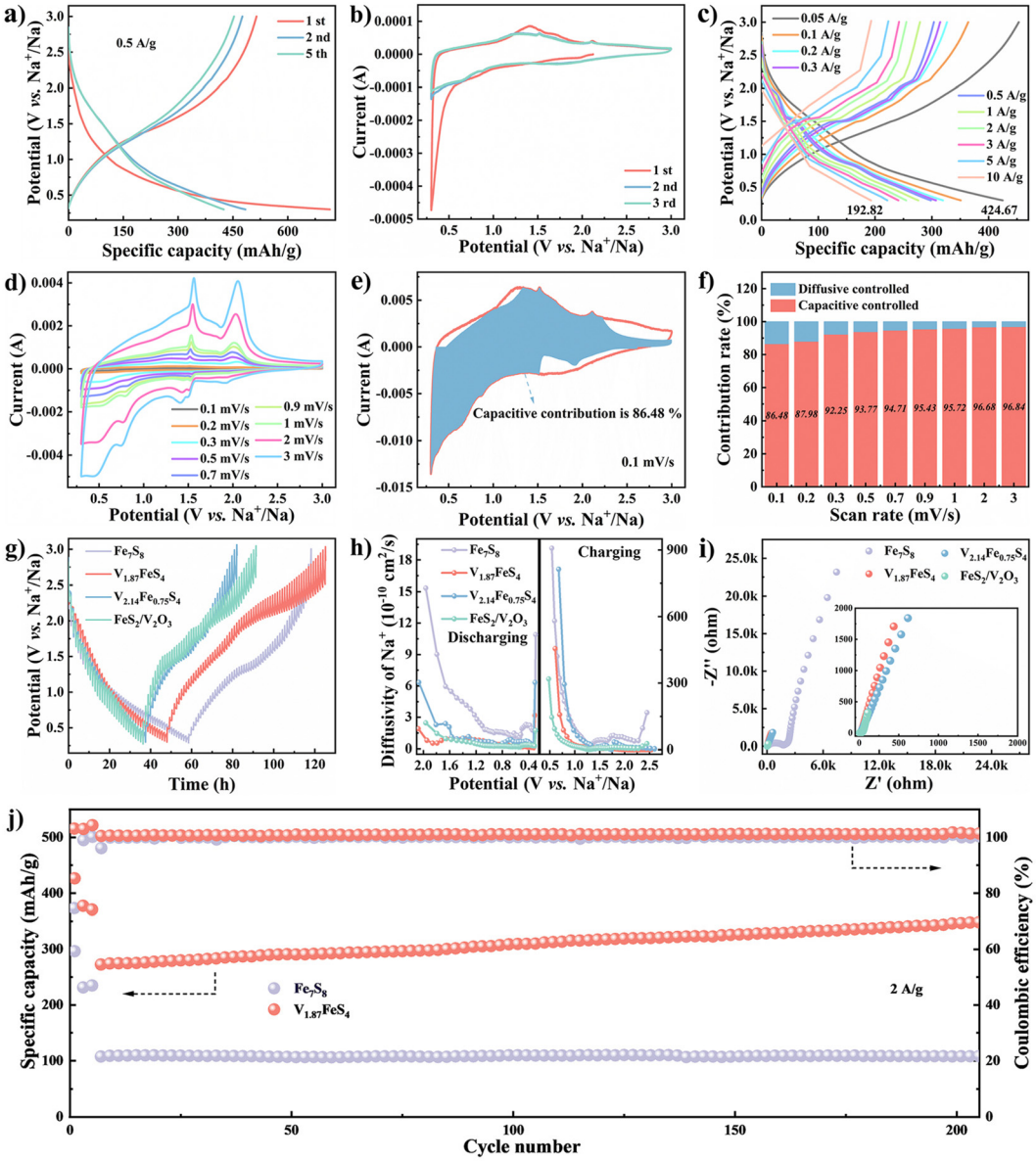

Fig. 5 Electrochemical performance of $V_{1.87}FeS_4$: (a) GCD profiles at 0.05 A g^{-1}, (b) CV curves at 0.1 mV s^{-1}, (c) GCD profiles at different current densities, (d) CV curves at different scan rates, (e) separation of capacitive (shadow region) and diffusive controlled contributions at 0.1 mV s^{-1}, and (f) the percentages of capacitive and diffusive controlled contributions at different scan rates; compared electrochemical performance: (g) GITT curves, (h) diffusivity of Na^+, and (i) Nyquist plots of Fe_7S_8, $V_{1.87}FeS_4$, $V_{2.14}Fe_{0.75}S_4$, and FeS_2/V_2O_3, (j) cycling performance at 2 A g^{-1} of Fe_7S_8 and $V_{1.87}FeS_4$.

tent titration technique (GITT) at a pulse current of 0.025 A g^{-1} (Fig. 5g), and the specific Na^+ diffusion coefficients (D_{Na^+}) were calculated in conjunction with eqn (3):

$$D_{Na^+} = \frac{4}{\pi \cdot \tau}\left(\frac{m_B \cdot V_m}{M_B \cdot S}\right)^2\left(\frac{\Delta E_s}{\Delta E_t}\right)^2 \quad (3)$$

where τ is for the pulse duration, m_B (g) and M_B denote the mass and molar mass of samples, V_m represents the molar volume, and S (cm^2) represents the area of the electrode. ΔE_s (V) presents the steady-state potential change due to the current pulse, and ΔE_t (V) presents the potential difference during the constant current pulse after eliminating the IR drop. As reflected in Fig. 5(h), D_{Na^+} of different samples are in the range of 10^{-9}–10^{-10} cm^2 s^{-1}. It is worth noting that D_{Na^+} is not consistent with the kinetic feature observed from CV curves, and even anomalies appear. In contrast, the result from EIS testing demonstrates the same Na^+ diffusion kinetics characteristics as CV testing. The EIS results reveal that Fe_7S_8 exhibits a larger semicircle in the high-frequency region compared to the other three materials. Moreover, a magnified view of the low-frequency region demonstrates that $V_{1.87}FeS_4$

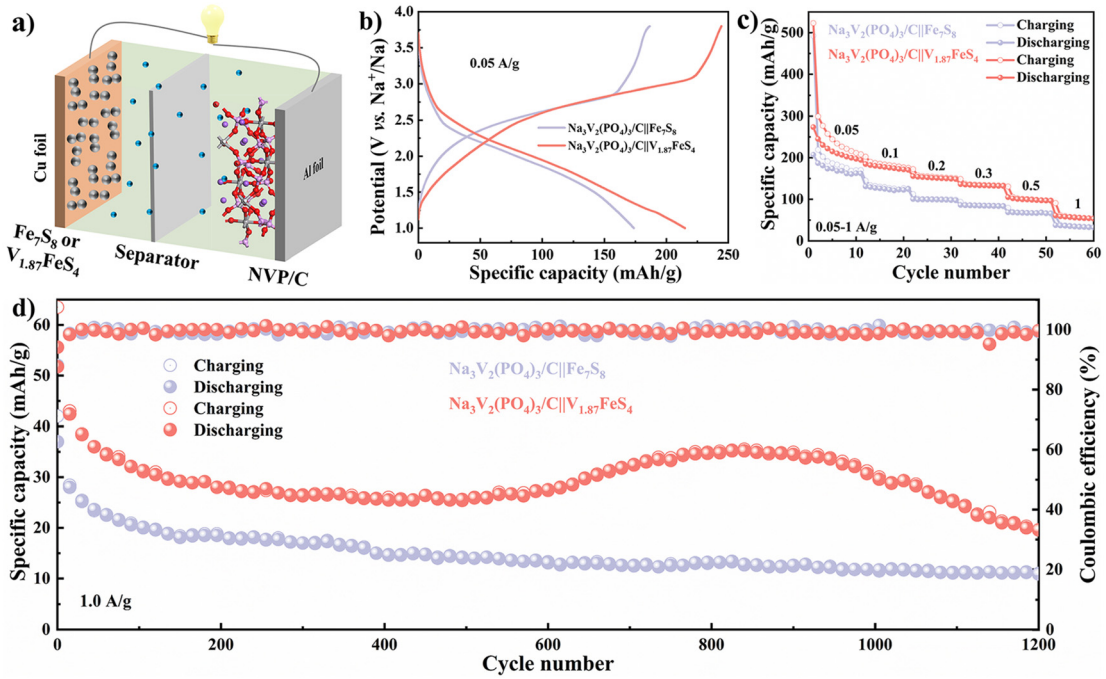

Fig. 6 Electrochemical performances of sodium-ion full-batteries: (a) the model of $Na_3V_2(PO_4)_3$/C||Fe_7S_8 or $V_{1.87}FeS_4$, (b) GCD curves at 0.05 A g^{-1}, (c) rate performances at various current densities, and (d) cycling performance at 1 A g^{-1}.

possesses the smallest diffusion impedance, which clearly indicates that it is conducive to the diffusion and transmission of sodium ions (Fig. 5i). This may be caused mainly by the shorter pulse duration setting during GITT testing, which must ensure that $\tau \ll L^2/D$ (L and D represent the diffusion length and coefficient, respectively).[46] In this work, the synthesized materials hold a micrometer scale and gradually change from a fluffy structure to a dense one with the introduction of the V source, so setting τ to 1 h may not be sufficient. This also illustrates the significance of choosing rational parameters based on the material during GITT testing. Given that $V_{1.87}FeS_4$ is equipped with a relatively faster Na^+ diffusion kinetics, superb specific capacity, and electrochemical reversibility. The long cycling performance of $V_{1.87}FeS_4$ (batteries are subjected to activate for 5 cycles at 0.05 A g^{-1}) is compared to that of pristine Fe_7S_8 at a current density of 2 A g^{-1} (the discharging time of each cycle is around 7.50 min). As demonstrated in Fig. 5j, withstanding 200 cycles of repeated charging/discharging, $V_{1.87}FeS_4$ still maintains a specific capacity of 348.17 mAh g^{-1} along with a coulombic efficiency of 101.38%, whereas the specific capacity of Fe_7S_8 faded to 108.25 mAh g^{-1} accompanied by a coulombic efficiency of 100.35%.

Considering the practicality of materials, the sodium ion full-batteries were assembled with commercial $Na_3V_2(PO_4)_3$/C as the cathode and $V_{1.87}FeS_4$ or Fe_7S_8 as the anode (Fig. 6a). The typical charging/discharging curves of $Na_3V_2(PO_4)_3$||$V_{1.87}FeS_4$ or Fe_7S_8 are depicted in Fig. 6(b). Impressively, $Na_3V_2(PO_4)_3$||$V_{1.87}FeS_4$ exhibits a rosy charging/discharging capacity of 244.51/215.11 mAh g^{-1} with an 87.97% coulombic efficiency in the voltage range of 1.0–3.8 V at 0.05 A g^{-1}. While $Na_3V_2(PO_4)_3$||Fe_7S_8 only achieves a specific capacity of 186.60/173.89 mAh g^{-1} at the same current density (both current density and capacity are calculated based on the mass of the anode material). Furthermore, $Na_3V_2(PO_4)_3$||$V_{1.87}FeS_4$ could maintain a significantly higher reversible capacity than $Na_3V_2(PO_4)_3$||Fe_7S_8 when the current density was increased to 1 A g^{-1} (Fig. 6c). The cycling lifespan of $Na_3V_2(PO_4)_3$||$V_{1.87}FeS_4$ full-batteries features outstanding cycling behavior after 1200 cycles of charging/discharging at a current density of 1 A g^{-1} (Fig. 6d). Accordingly, the excellent rate performance and long-term cycling stability of $Na_3V_2(PO_4)_3$||$V_{1.87}FeS_4$ suggests promising potential practical applications. Table S5 in the SI presents the cycling performance of the full-batteries in comparison with that reported previously.

4. Conclusions

In conclusion, iron/vanadium bimetallic sulfides were synthesized through *in situ* modulation of phase structure *via* sodium species based on their role in regulating the electron density of the Fe atom. It was noted that iron/vanadium bimetallic sulfides with varied phase structures could be obtained by adjusting the mass ratio of $Fe(NO_3)_3{\cdot}9H_2O$ and $NaVO_3$. Meanwhile, the existence of sodium species could reduce the energy required for the formation of bimetallic sulfides. As a result, distinct materials exhibited various electrochemical behaviors as they were employed as SIB anodes. The study suggests that $V_{1.87}FeS_4$ possesses brilliant Na^+ storage

capacity (the specific capacity is 424.67 mAh g^{-1} at 0.05 A g^{-1} and remains 192.82 mAh g^{-1} when the current density is increased 200-fold) when the mass ratio of $Fe(NO_3)_3{\cdot}9H_2O$ and $NaVO_3$ is 2 : 1. In addition, the full-batteries assembled with commercial $Na_3V_2(PO_4)_3/C$ also demonstrate remarkable electrochemical performance (43.4% capacity retention at 1 A g^{-1} after 1200 cycles). This work provides a novel, straightforward, and feasible preparation strategy for the development of micron-sized bimetallic sulfides applied to SIBs with fast-charging capability combined with the research in the field of catalysis.

Conflicts of interest

There are no conflicts to declare.

Data availability

Data will be available while required.

Supplementary information incorporates the XRD patterns, XPS spectra, element analysis, BET test, and electrochemical performance of different samples. See DOI: **https://doi.org/10.1039/d5eb00127g**.

Acknowledgements

This work was partly supported by the National Natural Science Foundation of China (52463013 and 52073133), the Key Talent Project Foundation of Gansu Province, Joint fund between Shenyang National Laboratory for Materials Science and State Key Laboratory of Advanced Processing and Recycling of Nonferrous Metals (18LHPY002), the Program for Hongliu Distinguished Young Scholars in Lanzhou University of Technology, and the Incubation Program of Excellent Doctoral Dissertation-Lanzhou University of Technology.

References

1 A. Rudola, R. Sayers, C. J. Wright and J. Barker, Opportunities for moderate-range electric vehicles using sustainable sodium-ion batteries, *Nat. Energy*, 2023, **8**, 215–218.

2 G. B. Fernando, IUPAC top ten emerging technologies in chemistry 2022: discover the innovations that will transform energy, health, and materials science, to tackle the most urgent societal challenges and catalyse sustainable development, *Chem. Int.*, 2022, **44**, 4–13.

3 W. Q. Zhao, S. Y. Lei, J. X. Li, F. Jiang, T. J. Wu, Y. Yang, W. Sun, X. B. Ji and P. Ge, Modulating internal coordination configurations for high–density atomic antimony toward advanced fast–charging sodium–ion batteries, *Adv. Energy Mater.*, 2024, **14**, 2304431.

4 H. S. Zhao, J. J. Zhong, Y. L. Qi, K. Liang, J. B. Li, X. B. Huang, W. K. Chen and Y. R. Ren, 90 C fast-charge Na-ion batteries for pseudocapacitive faceted TiO_2 anodes based on robust interface chemistry, *Chem. Eng. J.*, 2023, **465**, 143032.

5 Y. H. Wan, B. Y. Huang, W. S. Liu, D. L. Chao, Y. G. Wang and W. Li, Fast–charging anode materials for sodium–ion batteries, *Adv. Mater.*, 2024, **36**, 2404574.

6 Y. Q. Li, A. Vasileiadis, Q. Zhou, Y. X. Lu, Q. S. Meng, Y. Li, P. Ombrini, J. B. Zhao, Z. Chen, Y. S. Niu, X. G. Qi, F. Xie, R. V. D. Jagt, S. Ganapathy, M. M. Titirici, H. Li, Q. L. Chen, M. Wagemaker and Y. S. Hu, Origin of fast charging in hard carbon anodes, *Nat. Energy*, 2024, **9**, 134–142.

7 C. Y. Lu, L. Liu, S. He, B. X. Li, Z. X. Du, H. F. Du, X. F. Wang, S. W. Zhang and W. Ai, A 2D metallic KCu_4S_3 anode for fast–charging sodium–ion batteries, *Adv. Energy Mater.*, 2024, **14**, 2401221.

8 Z. Ali, T. Zhang, M. Asif, L. N. Zhao, Y. Yu and Y. L. Hou, Transition metal chalcogenide anodes for sodium storage, *Mater. Today*, 2020, **35**, 131–167.

9 Y. C. Fu, J. Sun, Y. S. Zhang, W. Qu, W. C. Wang, M. Yao, Y. Zhang, Q. Wang and Y. F. Tang, Revealing Na^+–coordination induced failure mechanism of metal sulfide anode for sodium ion batteries, *Angew. Chem., Int. Ed.*, 2024, **63**, e202403463.

10 T. Q. He, X. Y. Kang, L. Wang, Y. L. Yang, Q. H. Wu, Y. Y. Peng and F. Ran, Vanadium nitride induced method to construct cobalt sulfides homologous heterojunction toward ultrafast and high-capacity sodium-ion storage, *Acta Mater.*, 2024, **274**, 119997.

11 P. H. Song, J. Yang, C. Y. Wang, T. Y. Wang, H. Gao, G. X. Wang and J. B. Li, Interface engineering of Fe_7S_8/FeS_2 heterostructure in situ encapsulated into nitrogen-doped carbon nanotubes for high power sodium-ion batteries, *Nano–Micro Lett.*, 2023, **15**, 118.

12 H. Cai, F. Wang, H. Y. Feng, Z. D. Liu, C. Z. Zhang, A. B. Lu, X. Zhao, Q. H. Lu, Q. B. Liu and J. Tan, Boosting reaction kinetics of polycrystalline phase Fe_7S_8/FeS_2 heterostructures encapsulated in hollow carbon nanofibers for superior fast sodium storage, *J. Mater. Chem. A*, 2024, **12**, 11266–11276.

13 N. T. Wu, Z. B. Zhao, R. Hua, X. T. Wang, Y. M. Zhang, J. Li, G. L. Liu, D. L. Guo, G. Sun, X. M. Liu and J. W. Zhang, Predoping of dual-functional sodium to weaken Fe-S bond and stabilize interfacial chemistry for high-rate reversible sodium storage, *Adv. Energy Mater.*, 2024, **14**, 2400371.

14 L. C. Yue, W. Song, Z. G. Wu, W. X. Zhao, L. C. Zhang, Y. S. Luo, D. D. Zheng, B. H. Zhong, Q. Liu, S. J. Sun, X. D. Guo and X. P. Sun, Constructing FeS_2/TiO_2 p-n heterostructure encapsulated in one-dimensional carbon nanofibers for achieving highly stable sodium-ion battery, *Chem. Eng. J.*, 2023, **455**, 140824.

15 F. Fu, M. Hu, J. L. Key, P. K. Shen and J. L. Zhu, Carbon encapsulated FeS nanosheet-nanoribbon interwoven sandwich structure as efficient sodium-ion battery anodes, *Carbon*, 2023, **215**, 118469.

16 J. Liu, K. X. Zheng, Y. B. Mu, Z. Y. Zou, M. S. Han, C. F. Deng, J. C. Guo, F. H. Yu, W. J. Li, L. Wei, L. Zeng and T. S. Zhao, Nanosheet-interwoven structures and ion-electron decoupling storage enable $Fe_{1-x}S$ fast ion transport in $Li^+/Na^+/K^+$ batteries, *Nano Energy*, 2024, **131**, 110266.

17 S. Chen, S. Z. Huang, J. P. Hu, S. Fan, Y. Shang, M. E. Pam, X. X. Li, Y. Wang, T. T. Xu, Y. M. Shi and H. Y. Yang, Boosting sodium storage of $Fe_{1-x}S/MoS_2$ composite via heterointerface engineering, *Nano–Micro Lett.*, 2019, **11**, 80.

18 B. C. Chen, J. W. Ding, X. R. Bai, H. W. Zhang, M. Liang, S. Zhu, C. S. Shi, L. Y. Ma, E. Z. Liu, N. Q. Zhao, F. He, W. Zhou and C. N. He, Engineering pocket–like graphene-shell encapsulated FeS_2: inhibiting polysulfides shuttle effect in potassium–ion batteries, *Adv. Funct. Mater.*, 2022, **32**, 2109899.

19 D. Chen, X. W. Miao, J. Liu, J. T. Geng, L. Zhang, Z. F. Dai, H. L. Dong, J. Yang and H. B. Geng, Microspherical copper tetrathiovanadate with stable binding site as ultra-rate and extended longevity anode for sodium-ion half/full batteries, *Chem. Eng. J.*, 2022, **446**, 136772.

20 S. J. Li, P. Ge, F. Jiang, H. L. Shuai, W. Xu, Y. L. Jiang, Y. Zhang, J. G. Hu, H. S. Hou and X. B. Ji, The advance of nickel-cobalt-sulfide as ultra-fast/high sodium storage materials: the influences of morphology structure, phase evolution and interface property, *Energy Storage Mater.*, 2019, **16**, 267–280.

21 H. Pandey, P. Chithaiah, S. Vishwanathan, H. S. S. R. Matte and C. N. R. Rao, Topochemically synthesized Nb_3VS_6 as a stable anode for sodium-ion batteries, *Chem. Commun.*, 2024, **60**, 10017–10020.

22 Y. V. Lim, S. Z. Huang, Q. Y. Wu, D. Z. Kong, Y. Wang, Y. F. Zhu, Y. X. Wang, Y. X. Wang, H. K. Liu, S. X. Dou, L. K. Ang and H. Y. Yang, Super kinetically pseudocapacitive $MnCo_2S_4$ nanourchins toward high–rate and highly stable sodium–ion storage, *Adv. Funct. Mater.*, 2020, **30**, 1909702.

23 Z. Q. Hao, N. Dimov, J. K. Chang and S. Okada, Synthesis of bimetallic sulfide $FeCoS_4$@carbon nanotube graphene hybrid as a high-performance anode material for sodium-ion batteries, *Chem. Eng. J.*, 2021, **423**, 130070.

24 S. K. Jung, I. Hwang, D. Chang, K. Y. Park, S. J. Kim, W. M. Seong, D. Eum, J. Park, B. Kim, J. Kim, J. H. Heo and K. Kang, Nanoscale phenomena in lithium-ion batteries, *Chem. Rev.*, 2020, **120**, 6684–6737.

25 D. Yan, S. Z. Huang, Y. V. Lim, D. L. Fang, Y. Shang, M. E. Pam, J. Z. Yu, D. B. Xiong, X. L. Li, J. Zhang, Y. Wang, L. K. Pan, Y. Bai, Y. M. Shi and H. Y. Yang, Stepwise intercalation-conversion-intercalation sodiation mechanism in $CuInS_2$ prompting sodium storage performance, *ACS Energy Lett.*, 2020, **5**, 3725–3732.

26 T. Q. He, X. Y. Kang, F. J. Wang, J. L. Zhang, T. Y. Zhang and F. Ran, Capacitive contribution matters in facilitating high power battery materials toward fast-charging alkali metal ion batteries, *Mater. Sci. Eng., R*, 2023, **154**, 100737.

27 Y. Xu, P. Zhai, Y. C. Deng, J. L. Xie, X. Liu, S. Wang and D. Ma, Highly selective olefin production from CO_2 hydrogenation on iron catalysts: a subtle synergy between manganese and sodium additives, *Angew. Chem., Int. Ed.*, 2020, **59**, 21736–21744.

28 R. W. Yao, B. Wu, Y. Yu, N. Liu, Q. Q. Niu, C. M. Li, J. Wei and Q. J. Ge, Regulating the electronic property of iron catalysts for higher alcohols synthesis from CO_2 hydrogenation, *Appl. Catal., B*, 2024, **355**, 124159.

29 Q. L. Wei, R. H. DeBlock, D. M. Butts, C. Choi and B. Dunn, Pseudocapacitive Vanadium–based materials toward high–rate sodium–ion storage, *Energy Environ. Mater.*, 2020, **3**, 221–234.

30 R. F. Wang, Y. S. Chen, X. Shang, B. L. Liang, X. Zhang, H. Y. Zhuo, H. M. Duan, X. N. Li, X. F. Yang, X. Su, Y. Q. Huang and T. Zhang, Reversing the selectivity of alkanes and alkenes in iron-based fischer-tropsch synthesis: the precise control and fundamental role of sodium promotor, *ACS Catal.*, 2024, **14**, 11121–11130.

31 R. Wang, L. Wang, R. Liu, X. Y. Li, Y. Z. Wu and F. Ran, "Fast-charging" anode materials for lithium-ion batteries from perspective of ion diffusion in crystal structure, *ACS Nano*, 2024, **18**, 2611–2648.

32 Y. T. Li, S. T. Wang, Y. H. Dong, Y. Yang, Z. T. Zhang and Z. L. Tang, Glass–ceramic–like vanadate cathodes for high–rate lithium–ion batteries, *Adv. Energy Mater.*, 2020, **10**, 1903411.

33 R. Y. Hong, B. Feng, L. L. Chen, G. H. Liu, H. Z. Li, Y. Zheng and D. G. Wei, Synthesis, characterization and MRI application of dextran-coated Fe_3O_4 magnetic nanoparticles, *Biochem. Eng. J.*, 2008, **42**, 290–300.

34 Q. P. Li, R. S. Deng, Y. X. Chen, J. Gong, P. Wang, Q. J. Zheng, Y. Huo, F. Y. Xie, X. J. Wei, C. H. Yang and D. M. Lin, Homologous heterostructured NiS/NiS_2@C hollow ultrathin microspheres with interfacial electron redistribution for high–performance sodium storage, *Small*, 2023, **19**, 2303642.

35 X. Zhang, W. Weng, H. Gu, Z. B. Hong, W. Xiao, F. Wang, W. Li and D. Gu, Versatile preparation of mesoporous single–layered transition–metal sulfide/carbon composites for enhanced sodium storage, *Adv. Mater.*, 2022, **34**, 2104427.

36 F. Wang, Z. D. Liu, H. Y. Feng, Y. C. Wang, C. Z. Zhang, Z. H. Quan, L. X. Xue, Z. X. Wang, S. H. Feng, C. Ye, J. Tan and J. S. Liu, Engineering C-S-Fe bond confinement effect to stabilize metallic–phase sulfide for high power density sodium–ion batteries, *Small*, 2023, **19**, 2302200.

37 D. Yang, S. P. Zhang, P. Yu, S. L. Cheng, Z. S. Yuan, Y. Jiang, W. P. Sun, H. G. Pan, Y. Z. Feng, X. H. Rui and Y. Yu, Structure engineering of vanadium tetrasulfides for high–capacity and high–rate sodium storage, *Small*, 2022, **18**, 2107058.

38 H. Y. Chen, P. F. Tian, L. K. Fu, S. Y. Wan and Q. M. Liu, Hollow spheres of solid solution $Fe_7Ni_3S_{11}$/CN as advanced anode materials for sodium ion batteries, *Chem. Eng. J.*, 2022, **430**, 132688.

39 J. W. Chen, L. Mohrhusen, G. Ali, S. H. Li, K. Y. Chung, K. A. Shamery and P. S. Lee, Electrochemical mechanism

investigation of Cu_2MoS_4 hollow nanospheres for fast and stable sodium ion storage, *Adv. Funct. Mater.*, 2019, **29**, 1807753.

40 S. H. Yang, S. K. Park, G. D. Park, J. H. Kim and Y. C. Kang, Rational synthesis of uniform yolk-shell Ni-Fe bimetallic sulfide nanoflakes@porous carbon nanospheres as advanced anodes for high-performance potassium-/sodium-ion batteries, *Chem. Eng. J.*, 2021, **417**, 127963.

41 B. Liu, D. Z. Kong, Y. Wang, Y. V. Lim, S. Z. Huang and H. Y. Yang, Three-dimensional hierarchical $NiCo_2S_4$@MoS_2 heterostructure arrays for high performance sodium ion battery, *FlatChem*, 2018, **10**, 14–21.

42 J. F. Li, J. Zhou, Q. H. Zhou, X. Wang, C. Guo and M. Li, Promoting the Na^+-storage of $NiCo_2S_4$ hollow nanospheres by surfacing Ni-B nanoflakes, *J. Mater. Sci. Technol.*, 2021, **82**, 114–121.

43 C. Y. Zhao, J. J. Dai, Z. F. Lu, R. Z. Fan, F. S. Zhu, J. Wu and Y. R. Cai, $FeCoS_2$ nanoparticles confined in N, S co-doped carbon with reduced polysulfides shuttling for high performance sodium-ion batteries, *Appl. Surf. Sci.*, 2023, **634**, 157711.

44 L. Chen, M. S. Wang, E. Z. Li, S. M. Huang, Q. Li, L. Yang, X. Hu, Z. L. Yang, J. C. Chen, Z. Y. Ma, B. S. Guo, B. Yu, Y. Huang and X. Li, Deciphering multistep transformation mechanism of cobalt-vanadium bimetallic sulfides anode in sodium storage, *J. Power Sources*, 2024, **603**, 234456.

45 Y. Rao, K. J. Zhu, G. L. Zhang, F. Dang, J. T. Chen, P. H. Liang, Z. H. Kong, J. Guo, H. J. Zheng, J. Zhang, K. Yan, J. S. Liu and J. Wang, Interfacial engineering of MoS_2/V_2O_3@C-rGO composites with pseudocapacitance-enhanced Li/Na-ion storage kinetics, *ACS Appl. Mater. Interfaces*, 2023, **15**, 55734–55744.

46 W. Weppner and R. A. Huggins, Determination of the kinetic parameters of mixed–conducting electrodes and application to the system Li_3Sb, *J. Electrochem. Soc.*, 1977, **124**, 1569.